
VOLUME 157 • ISSUE 12 • DECEMBER 2010
ELSEVIER
Combustion and Flame
THE JOURNAL OF THE COMBUSTION INSTITUTE
Available online at www.sciencedirect.com
ScienceDirect

Combustion and Flame 157 (2010) 2267–2276

Contents lists available at ScienceDirect

Combustion and Flame

journal homepage: www.elsevier.com/locate/combustflame

Effects of radiation and compression on propagating spherical flames of methane/air mixtures near the lean flammability limit

Zheng Chen *

State Key Laboratory for Turbulence and Complex Systems, Department of Mechanics and Aerospace Engineering, College of Engineering, Peking University, Beijing 100871, China

ARTICLE INFO

Article history:
Received 25 March 2010
Received in revised form 18 May 2010
Accepted 8 July 2010
Available online 3 August 2010

Keywords:
Laminar flame speed
Markstein length
Propagating spherical flame
Radiation
Compression

ABSTRACT

Large discrepancies between the laminar flame speeds and Markstein lengths measured in experiments and those predicted by simulations for ultra-lean methane/air mixtures bring a great concern for kinetic mechanism validation. In order to quantitatively explain these discrepancies, a computational study is performed for propagating spherical flames of lean methane/air mixtures in different spherical chambers using different radiation models. The emphasis is focused on the effects of radiation and compression. It is found that the spherical flame propagation speed is greatly reduced by the coupling between thermal effect (change of flame temperature or unburned gas temperature) and flow effect (inward flow of burned gas) induced by radiation and/or compression. As a result, for methane/air mixtures near the lean flammability limit, the radiation and compression cause large amounts of under-prediction of the laminar flame speeds and Markstein lengths extracted from propagating spherical flames. Since radiation and compression both exist in the experiments on ultra-lean methane/air mixtures reported in the literature, the measured laminar flame speeds and Markstein lengths are much lower than results from simulation and thus cannot be used for kinetic mechanism validation.

1. Introduction

The laminar flame speed and Markstein length are two fundamental parameters of a combustible mixture [1,2]. Their accurate determination is extremely important for validating chemical kinetic mechanisms [3] and for modeling turbulent premixed combustion within the laminar flamelet regime [4]. Therefore, in the last 50 years, substantial attention has been given to the determination of the laminar flame speed and Markstein length and various experimental approaches have been developed to measure these two parameters [5,6].

The most common approaches for measuring the laminar flame speed and Markstein length are the counterflow flame method [7,8] and the propagating spherical flame method [9–26]. Recently, Davis and coworkers [27,28] investigated the counterflow flames and found that the stretch rate measured at the position of local minimum flow velocity (or maximum velocity gradient) is not an accurate indicator of the stretch exerted on the flame. Therefore, it is difficult to accurately determine the Markstein length using the counterflow flame method [27,28]. Moreover, because of the Reynolds number limit, it is difficult to use the counterflow flame method to measure the laminar flame speed at high pressures [15]. Consequently, due to its simple flame configuration and well-defined flame stretch rate at normal and high pressures, the propagating spherical flame method is currently the most favorable method for measuring the laminar flame speed and Markstein length [9–26].

In the propagating spherical flame method, a quiescent homogeneous combustible mixture in a closed chamber is centrally ignited by an electrical spark which results in an outwardly propagating spherical flame [9–26]. The stretched flame speed and stretch rate are calculated from the flame front history, $R_f = R_f(t)$, which is recorded by schlieren or shadow photography. The unstretched laminar flame speed and Markstein length are then obtained from the linear extrapolation between the stretched flame speed and stretch rate. Recently, a great deal of effort has been devoted to obtaining accurate laminar flame speed and Markstein length from propagating spherical flames. For example, Bradley et al. [12] studied the effects of ignition and different isotherms on the spherical flame propagation speed; Qiao et al. [20] designed a short-drop free-fall laboratory facility that provides low gravity conditions (10^{-2} g) so that the effects of buoyancy can be minimized; Chen et al. [23] showed that the flame speed reverse phenomenon greatly narrows the experimental data range valid for flame speed extrapolation; Burke et al. [24] demonstrated that the flow field deviation due to non-spherical chambers can reduce the accuracy of flame speed measurements.

However, discrepancies among the laminar flame speeds and Markstein lengths measured by different researchers for the same

* Fax: +86 10 6275 7532.
E-mail address: cz@pku.edu.cn

0010-2180/$ - see front matter © 2010 The Combustion Institute. Published by Elsevier Inc. All rights reserved.
doi:10.1016/j.combustflame.2010.07.010

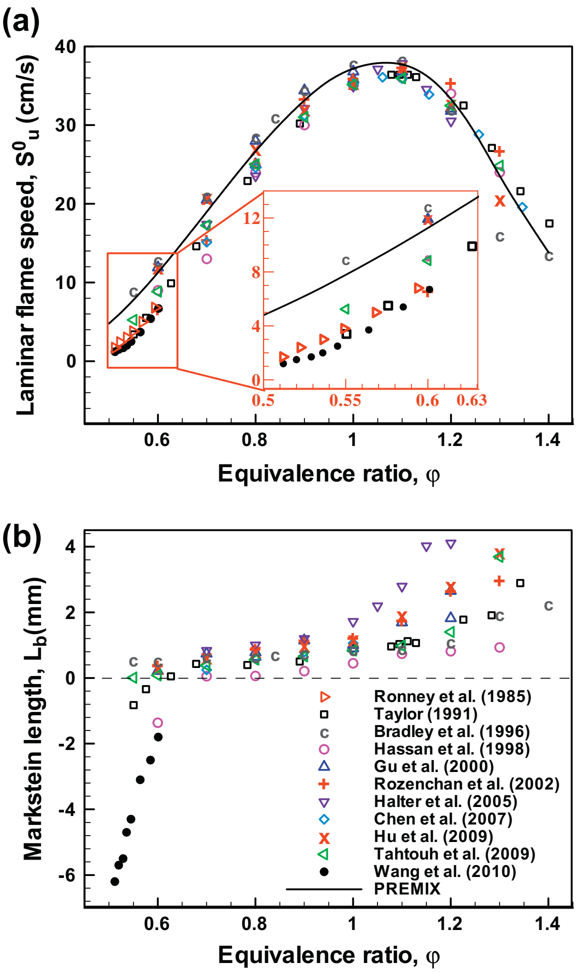

Fig. 1. (a) Laminar flame speed and (b) Markstein length relative to the burned gas for methane/air mixtures at atmospheric pressure and room temperature (symbols: results extracted from outwardly propagating spherical flames; line: results from simulation of adiabatic propagating planar flames).

fuel are still appearing in the literature [29,30] and become a great concern for kinetic mechanism validation. Figure 1 shows the measured laminar flame speeds, S_u^0, and the Markstein lengths relative to the burned gas, L_b, for the simplest hydrocarbon fuel, methane. Except for the laminar flame speed calculated by PREMIX (solid line) [31], all the experimental results (symbols) were measured using the propagating spherical flame method [10,14,16–18,21,22,25,26,32]. For near-stoichiometric and rich CH_4/air mixtures ($\varphi \geqslant 0.8$), relatively small discrepancies are shown to exist among the measured laminar flame speeds; unlike the laminar flame speeds, Fig. 1b shows that there are very large discrepancies for the Markstein lengths measured by different researchers and the relative difference can even be larger than 300% for $\varphi > 1.1$. For CH_4/air mixtures near the lean flammability limit ($\varphi \leqslant 0.65$), Fig. 1 shows that there are huge discrepancies among S_u^0 and L_b measured by different researchers and/or predicted from simulation. According to Ronney and Wachman [32], the buoyancy strongly affects the spherical flame propagation in normal-gravity experiments when S_u^0 is below 15 cm/s. Therefore, micro-gravity experiments should be conducted for methane/air mixtures near the lean flammability limit ($\varphi \leqslant 0.65$). In Fig. 1, only results reported by Ronney and Wachman [32] and Wang et al. [26] were obtained from micro-gravity experiments. Though good agreement is achieved for the laminar flame speeds measured in micro-gravity experiments [26,32], the measured data are much lower than numerical prediction, as shown in the enlarged inset in Fig. 1a. Furthermore, Fig. 1b shows that the negative Markstein lengths reported by Wang et al. [26] were unreasonably lower than those measured by other researchers and predicted by simulation (It is noted that in Ref. [32], the stretched flame speed at $R_f = 7$ cm was considered to be the laminar flame speed. Linear extrapolation to zero stretch rate was not conducted and thus the Markstein length was not obtained by Ronney and Wachman [32].)

The reason for these discrepancies has yet to be quantitatively explained. The difference between experimental and numerical results mentioned above could be caused by the inaccuracy of the experimental measurements, the inaccuracy of the theoretical models employed in the data processing, or/and the invalidity of the kinetic mechanism. In this study, numerical simulation is conducted to help understand the deficiencies of the models used to interpret the experimental measurement. For lean CH_4/air mixtures, there are two possible sources affecting the accuracy of the measured S_u^0 and L_b. The first one is radiation, which always exits in experiments and is important for spherical flames of near-limit mixtures [33,34]. The second one is compression, which is caused by pressure increase during the flame propagation and is important for spherical flame experiments conducted in a small chamber [35]. The objective of this study is to assess the effects of radiation and compression on the flame propagation speed and the extracted laminar flame speed and Markstein length. The effects of radiation and compression were not accounted for in the interpretation of experimental measurements. In this study, they are found to be the causes for the discrepancies between measured and calculated S_u^0 and L_b of CH_4/air mixtures near the lean flammability limit.

The paper is organized as follows: in Section 2, numerical methods and specifications are presented; then, in Section 3, the radiation and compression effects on the flame propagation speed and linear extrapolation are assessed and the radiation re-absorption effects are discussed; finally, the conclusions are summarized in Section 4.

2. Numerical methods and specifications

In order to study the effects of radiation and compression on spherical flame propagation, a time-accurate and space-adaptive numerical solver for Adaptive Simulation of Unsteady Reactive Flow, A-SURF (1D), is used to carry out high-fidelity numerical simulation of outwardly propagating spherical flames. A-SURF has been successfully used and validated in a series of studies on spherical flame initiation and propagation [23,24,30,35,36].

The unsteady Navier–Stokes equations and the energy and species conservation equations for a multi-species reactive mixture in a one-dimensional spherical coordinate are solved in A-SURF [23]:

$$\frac{\partial U}{\partial t} + \frac{1}{r^2}\frac{\partial F(U)}{\partial r} = \frac{1}{r^2}\frac{\partial F_v(U)}{\partial r} + S_R \tag{1}$$

where the vectors U, $F(U)$, $F_v(U)$, and S_R are defined as

$$U = \begin{pmatrix} \rho Y_1 \\ \rho Y_2 \\ \vdots \\ \rho Y_n \\ \rho u \\ E \end{pmatrix}, \quad F(U) = \begin{pmatrix} r^2 \rho u Y_1 \\ r^2 \rho u Y_2 \\ \vdots \\ r^2 \rho u Y_n \\ r^2(\rho u^2 + P) \\ r^2(E+P)u \end{pmatrix},$$

$$F_v(U) = \begin{pmatrix} -r^2 \rho Y_1 V_1' \\ -r^2 \rho Y_2 V_2' \\ \vdots \\ -r^2 \rho Y_n V_n' \\ r^2 \tau_1 \\ r^2 q \end{pmatrix}, \quad S_R = \begin{pmatrix} \omega_1 \\ \omega_2 \\ \vdots \\ \omega_n \\ -2\tau_2/r \\ q_r \end{pmatrix} \tag{2}$$

Here ρ is the density, u the flow velocity in the radial direction, and E the total energy per unit mass. Instead of solving the continuity equation, the species conservation equations for all n species are solved in A-SURF. The quantities, Y_k, V'_k and ω_k, are the mass fraction, diffusion velocity and production rate of species k, respectively. The production rate of species k, ω_k, due to chemical reaction is specified via collection of elementary reactions using a CHEMKIN compatible database [37]. The mixture-averaged formula [31] is employed to calculate diffusion velocity, in which the thermal diffusion of H and H_2 is considered. Moreover, a correction velocity is included to ensure the mass conservation [31].

In the momentum equation, P is the hydrostatic pressure, and the viscous stresses, τ_1 and τ_2, in the one-dimensional spherical coordinate are

$$\tau_1 = \frac{2\mu\partial u}{\partial r} - \frac{2\mu}{3r^2}\frac{\partial(r^2 u)}{\partial r}, \quad \tau_2 = \frac{2\mu u}{r} - \frac{2\mu}{3r^2}\frac{\partial(r^2 u)}{\partial r} \tag{3}$$

where μ is the dynamic viscosity of the mixture.

In the energy conservation equation, the total energy, E, is defined through

$$E = -P + \rho u^2/2 + \rho h, \quad h = \sum_{k=1}^{n}(Y_k h_k), \quad h_k = h_{k,0} + \int_{T_0}^{T} C_{P,k}(T)dT, \tag{4}$$

where T is the temperature, h_k, the enthalpy of species k, $h_{k,0}$ the species enthalpy of formation at the reference temperature T_0, and $C_{P,k}$ the specific heat of species k at constant pressure. The heat flux is

$$q = \lambda\frac{\partial T}{\partial r} - \rho\sum_{k=1}^{n}(h_k Y_k V'_k) \tag{5}$$

where λ is the thermal conductivity of the gas mixture. The radiative source term, q_r, in the energy conservation equation is evaluated according to different radiation models discussed later.

Details on the numerical schemes and code validation of A-SURF can be found in Ref. [23] and hence are only briefly described below. The finite volume method is used to discretize the conservation governing equations in the spherical coordinate. The second-order accurate, Strang splitting fractional-step procedure [38] is utilized to separate the time evolution of the stiff reaction term from that of the convection and diffusion terms. In the first fractional step, the non-reactive flow is solved. The Runge–Kutta, MUSCL-Hancock, and central difference schemes, all of second-order accuracy, are employed for the calculation of the temporal integration, convective flux, and diffusive flux, respectively. The chemistry is solved in the second fractional step using the VODE solver [39]. The detailed methane/air reaction mechanism, GRI-MECH 3.0 [40], is used in this study. The chemical reaction rates as well as thermodynamic and transport properties are evaluated using the CHEMKIN and TRANSPORT packages [31,37] interfaced with A-SURF.

In order to assess the radiation effects, we employ three different radiation models in the simulation. The first one is the adiabatic model (denoted by 'ADI') in which radiation is not considered. The second one is the optically thin model (denoted by 'OTM') in which only the radiation emission from CO_2, H_2O, CO, and CH_4 is considered [41]. The optically thin model basically assumes that radiation can pass through the medium without significant absorption. However, it is well known that CO_2 is not only a radiation emitter but also a strong absorber. Therefore, more accurate radiation model should be considered. To account for the radiative transport including both emission and re-absorption, the third radiation model, statistical narrow band model (denoted by 'SNB'), is also used in this study. The fitted statistical narrow-band correlated-k (FSNB-CK) method [42] is employed to calculate the radiative transport in the third radiation model. The details on the numerical algorithm and model accuracy of FSNB-CK can be found in Ref. [42] and thus are not repeated here. In order to investigate the compression effects, simulations of propagating flames in two spherical chambers of different radii, R_w = 4.96 cm (small one, denoted by 'S') and R_w = 100 cm (large one, denoted by 'L'), are conducted. In the micro-gravity experiments conducted by Wang et al. [26], the chamber volume is $V = 8 \times 8 \times 8$ cm^3 and its equivalent radius is $R_w=(3V/4\pi)^{1/3}$ = 4.96 cm. Therefore, simulation results for R_w = 4.96 cm can be compared directly with the experimental data reported in Ref. [26]. For R_w = 100 cm, the relative pressure increase (which is proportional to the ratio between the volume of burned gas and that of the chamber) is below 0.15‰ and thus the compression effects are negligible when the flame radius is less than 5 cm [35].

In simulation, the expanding spherical flame is initiated by a hot pocket (1–2.5 mm in radius) of burned product surrounded by fresh mixture at room temperature (T_u = 298 K). The size of the hot pocket is chosen so that the effects of ignition can be minimized [12,23]. The initial wall temperature is 298 K. The initial pressure and flow velocity at every grid are 1 atm and 0 cm/s, respectively. To accurately and efficiently resolve the propagating spherical flame, a multi-level, dynamically adaptive mesh is used in A-SURF and the flame front is always fully covered by the finest grids of 16 μm in width. The grid refining and coarsening procedures introduced by Sun and Takayama [43] are employed in A-SURF. For R_w = 4.96 cm, six grid levels (from level 0 to level 5) are utilized (thus the largest mesh size is 16×2^5 = 512 μm) and the total number of grid points is around 200. For R_w = 100 cm, nine grid levels (from level 0 to level 8) are utilized (thus the largest grid size is 16×2^8 = 4096 μm) and the total number of grid points is about 360. For both cases, R_w = 4.96 cm and R_w = 100 cm, the number of the finest grid covering the moving flame front is around 100. When a uniform grid of 16 μm is used in the simulation, the mesh number for R_w = 4.96 cm and R_w = 100 cm is 3100 and 62,500, respectively. Therefore, a speed-up of 3100/200 = 15.5 and 62,500/360 = 173.6 is achieved with the help of adaptive mesh. Figure 2 shows the grid level distribution for R_w = 4.96 cm. The flame front position is R_f = 0.9 cm. It is seen that the flame front is always fully covered by the finest grids at level L = 5. Furthermore, Fig. 2 shows that the inner (r = 0) and outer ($r = R_w$) boundaries are also covered by finest grids, with the help of which the boundary conditions (shown in Fig. 2) can be satisfied in the simulation. Since the finite volume method is used, at r = 0 only the convective and diffusive fluxes need to be calculated and the singularity problem is avoided. At $r = R_w$, the wall is considered to be adiabatic and the wall effect on radiation transportation is not considered in this study. Grid convergence is tested to ensure the numerical accuracy: the relative change of the flame propagation speed is found to be within 0.5% when the size of the finest grid is halved (i.e. 8 μm in width).

3. Results and discussion

Propagating spherical flames of lean CH_4/air mixtures in two spherical chambers, R_w = 4.96 cm (S) and R_w = 100 cm (L), are simulated using three radiation models, ADI, OTM, and SNB. In the results presented below, the chamber size and radiation model are indicated by different abbreviations listed in Table 1. By comparing the results from L-OTM/S-ADI with and those from L-ADI, the radiation/compression effects can be assessed (the effects of radiation re-absorption are investigated only in the last sub-section via comparison among results from L-ADI, L-OTM, and L-SNB). Nine different CH_4/air mixtures are studied and the equivalence ratios, φ = 0.5, 0.52, 0.536, 0.55, 0.564, 0.585, 0.6, 0.65, and

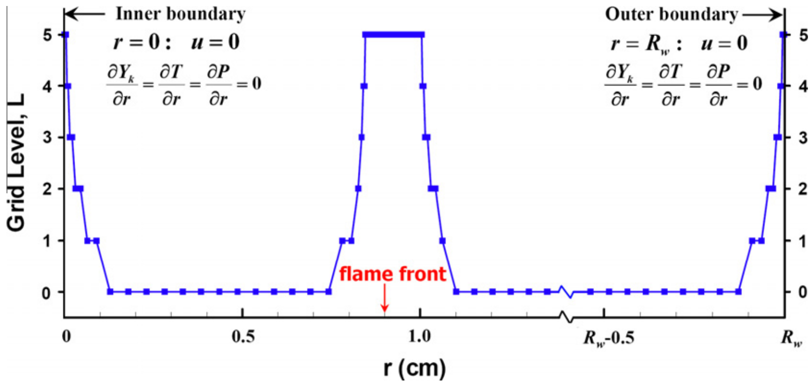

Fig. 2. Grid level distribution on the computational domain of $0 \leqslant r \leqslant R_w$. The boundary conditions are presented. The size of a grid at level L is $512/2^L$ μm.

Table 1
The corresponding chamber size and radiation model for different abbreviations.

	Chamber size, R_w (cm)	Radiation model
S-ADI	4.96	Adiabatic model
S-OTM	4.96	Optically thin model
L-ADI	100	Adiabatic model
L-OTM	100	Optically thin model
L-SNB	100	Statistical narrow band model

0.7, are chosen so that some of the numerical results can be compared with the experimental data reported in Ref. [26].

3.1. Radiation and compression effects on flame propagation speed

From the flame front history, $R_f = R_f(t)$, defined as the position of maximum heat release rate in the simulation, the flame propagation speed, S, can be calculated via numerical differentiation, i.e. $S = dR_f/dt$. Figure 3 shows the flame propagation speeds of lean CH_4/air mixtures near the flammability limit. In Fig. 3a, S is shown to monotonically increase with R_f when both radiation and compression are excluded (L-ADI). When radiation is considered (L-OTM), S still monotonically increases with R_f. However, due to the radiation effects, it is lower than that without radiative loss (L-ADI). The difference between the flame propagation speeds for adiabatic and radiative cases is shown to increase with the flame radius. When the smaller chamber is considered (S-OTM), S is shown to first increase and then decrease with R_f. This is due to the fact that, with the increase of flame radius, the pressure increases and the flame propagation speed will be affected by the compression effect [35]. It is seen that the difference between the flame propagation speeds from S-OTM and L-OTM increases quickly with the flame radius. Therefore, both radiation and compression reduce the flame propagation speed and the larger the flame radius, the stronger the radiation and compression effects.

The experimental results reported in Ref. [26] are also presented in Fig. 3 for comparison. It is seen that S measured in the micro-gravity experiments [26] monotonically decreases with R_f, which is in the opposite trend to those predicted by simulations for L-ADI and L-OTM. Since a chamber with equivalent radius of $R_w = (3V/4\pi)^{1/3} = 4.96$ cm was used in the experiments [26], the compression effects, as demonstrated by simulation results for S-OTM, slow down the flame propagation when the flame radius is large. Therefore, it is reasonable that the measured S decreases with R_f for large flame radius ($R_f > 1.5$ cm). However, it is not clear why the measured S decreases with R_f when the flame radius is small ($R_f < 1.5$ cm), for which the compression effects are almost negligible (the relative pressure increase is below 3% when $R_f/R_w < 1.5/4.96 \approx 0.3$ [35]). One possible reason could be that the spark ignition still affects the flame propagation even when the flame radius is between 1.0 and 1.5 cm [23].

The flame propagation speed as a function of stretch rate, $K=(2/R_f)dR_f/dt = 2S/R_f$, is shown in Fig. 3b. Simulation results show that S decreases monotonically with K only for L-ADI, while S changes non-monotonically with K for L-OTM (due to the radiation effects), S-ADI (due to the compression effects), and S-OTM (due to the compression and radiation effects). However, the measured S increases linearly with K [26]. Consequently, as shown by Fig. 3b, there is huge difference among the extracted flame propagation speeds at zero stretch rate from simulations and experiments. In fact, because of the compression effects (S-ADI and S-OTM), the linear extrapolation between S and K cannot be conducted to get S at $K = 0$.

In order to explain why the flame propagation speed is reduced by the radiation and compression effects, the evolution of temperature and flow velocity is plotted in Fig. 4 for spherical CH_4/air ($\varphi = 0.585$) flames. For L-ADI without radiation and compression, the temperature of burned and unburned mixtures is nearly constant and the flow velocity of the burned gas just behind the flame front is zero ($U_b = 0$). When radiation is considered (L-OTM), the flame temperature is reduced by about 20–30 K, resulting in a lower flame propagation speed. Meanwhile, due to radiation cooling, the burned gas temperature decreases during the flame propagation and the burned gas moves toward the center ($U_b < 0$). Therefore, there are two effects affecting S: (1) the thermal effect by which the flame temperature and thus S are reduced due to the radiative heat loss; and (2) the flow effect by which S is reduced by the incoming flow of burned gas ($U_b < 0$) caused by the radiation cooling.

When compression is considered (S-ADI), the temperature of unburned gas increases during the flame propagation. Therefore, the flame becomes stronger and should propagate faster. However, due to the pressure rise, the burned gas moves toward the center ($U_b < 0$) and thus the flame propagation will be slowed down. Therefore, there are also two effects affecting S: (1) the thermal effect by which the unburned gas temperature and thus S increase due to compression; and (2) the flow effect by which S is reduced by the incoming flow of burned gas ($U_b < 0$) caused by compression. Simulation results show that the flow effect is stronger than the thermal effect. Therefore, similar to the radiation effects, the compression effects also reduce the spherical flame propagation speed. When both radiation and compression are considered (S-OTM), the temperature of unburned mixture is smaller than that for S-ADI while the temperature of burned gas is larger than that for L-OTM. This is because temperature decreases due to radiation while it increases due to compression. Since both radiation and compression cause inward flow of burned gas, the magnitude

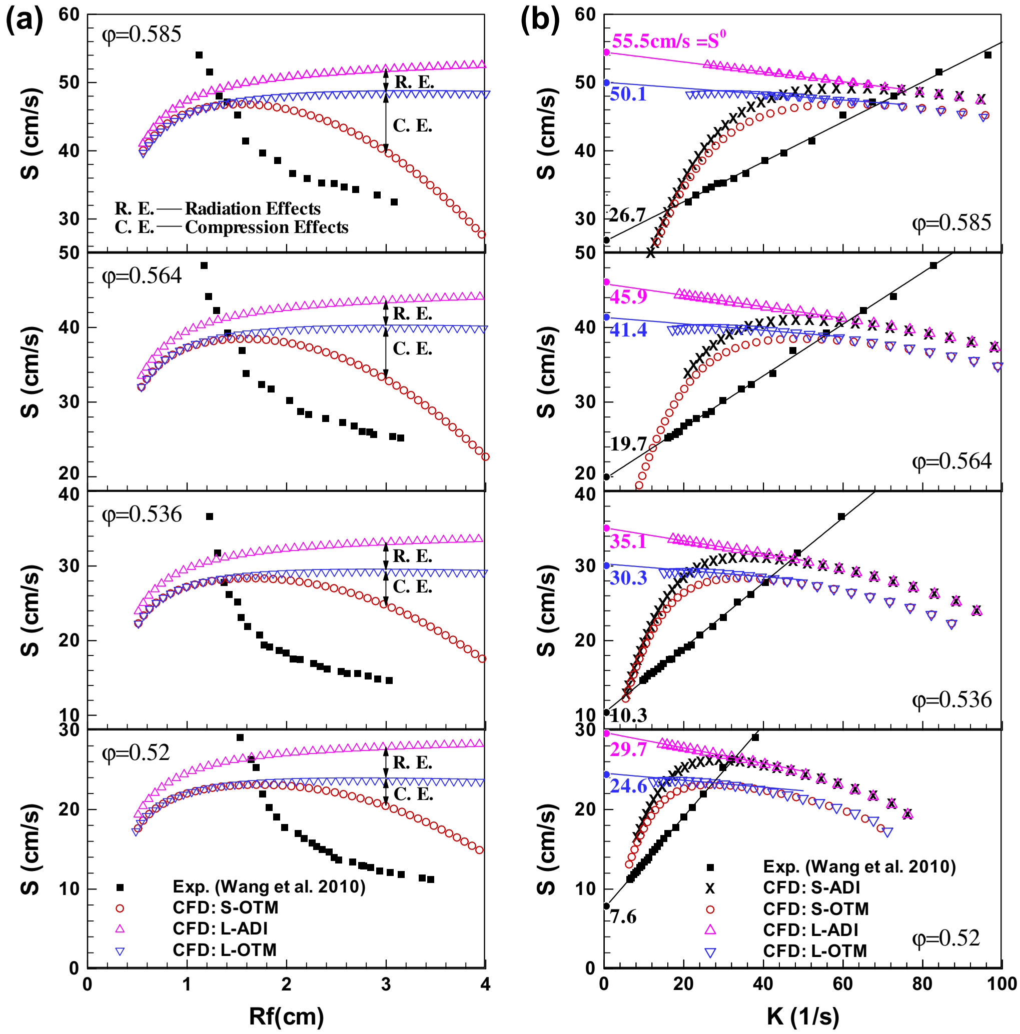

Fig. 3. Flame propagation speed as a function of: (a) flame radius and (b) stretch rate. The lines in figure (b) stand for linear extrapolations and the extracted results at zero stretch rate are presented.

of burned gas velocity for S-OTM is shown to be larger than those for S-ADI and L-OTM.

Figure 5 shows U_b as a function of R_f. U_b is chosen as the flow velocity at the position where 99.9% of the total heat release occurs and it is very close (the relative difference is within 0.5%) to the minimum flow velocity shown in Fig. 4b. The magnitude of the radiation induced inward flow is seen to increase with the flame radius (Fig. 5a). This explains why the difference between the flame propagation speeds for adiabatic and radiative cases increases with the flame radius (comparing results for L-OTM and L-ADI in Fig. 3a). Figure 5b shows that the compression induced inward flow increases exponentially with the flame radius. This explains why the difference between the flame propagation speeds from S-OTM and L-OTM increases quickly with the flame radius (comparing results for S-OTM and L-OTM in Fig. 3a). It is seen that the compression induced velocity is two to three times larger than the radiation induced velocity. Therefore, the flow effect on S due to compression is much stronger than that due to radiation.

Summarizing, both radiation losses and compression reduce the flame propagation speed. With the increase of the flame radius, the radiation and compression effects are found to become stronger. Moreover, it is demonstrated that the reduction of the flame propagation speed is due to the coupling between the thermal and flow effects caused by radiation or compression.

3.2. Radiation and compression effects on the linear extrapolation

In the propagating spherical flame method, the unstretched laminar flame speed and Markstein length can be extracted from the linear extrapolation based on the following correlation [1]

$$S_b = S_b^0 - L_b K \tag{6}$$

where S_b, S_b^0, and L_b are, respectively, the stretched flame speed, unstretched flame speed, and Markstein Length, all relative to the burned mixture. It is noted that the Markstein length (L_b) is for the stretched flame speed relative to the burned mixture (S_b), which is not equal to the consumption speed or the displacement speed defined in Ref. [46]. Knowing S_b^0, the unstretched laminar flame speed relative to the unburned mixture, S_u^0, can be deduced through mass conservation: $S_u^0 = \sigma S_b^0$, where σ is the density ratio between the burned and unburned mixtures.

According to the kinetic balance with respect to the burned mixture, the stretched flame speed is

$$S_b = S - U_b \tag{7}$$

In all the previous experiments utilizing the spherical flame method to measure S_u^0 and L_b (Fig. 1 and references therein), the burned gas was assumed to be quiescent ($U_b \approx 0$) and thus the

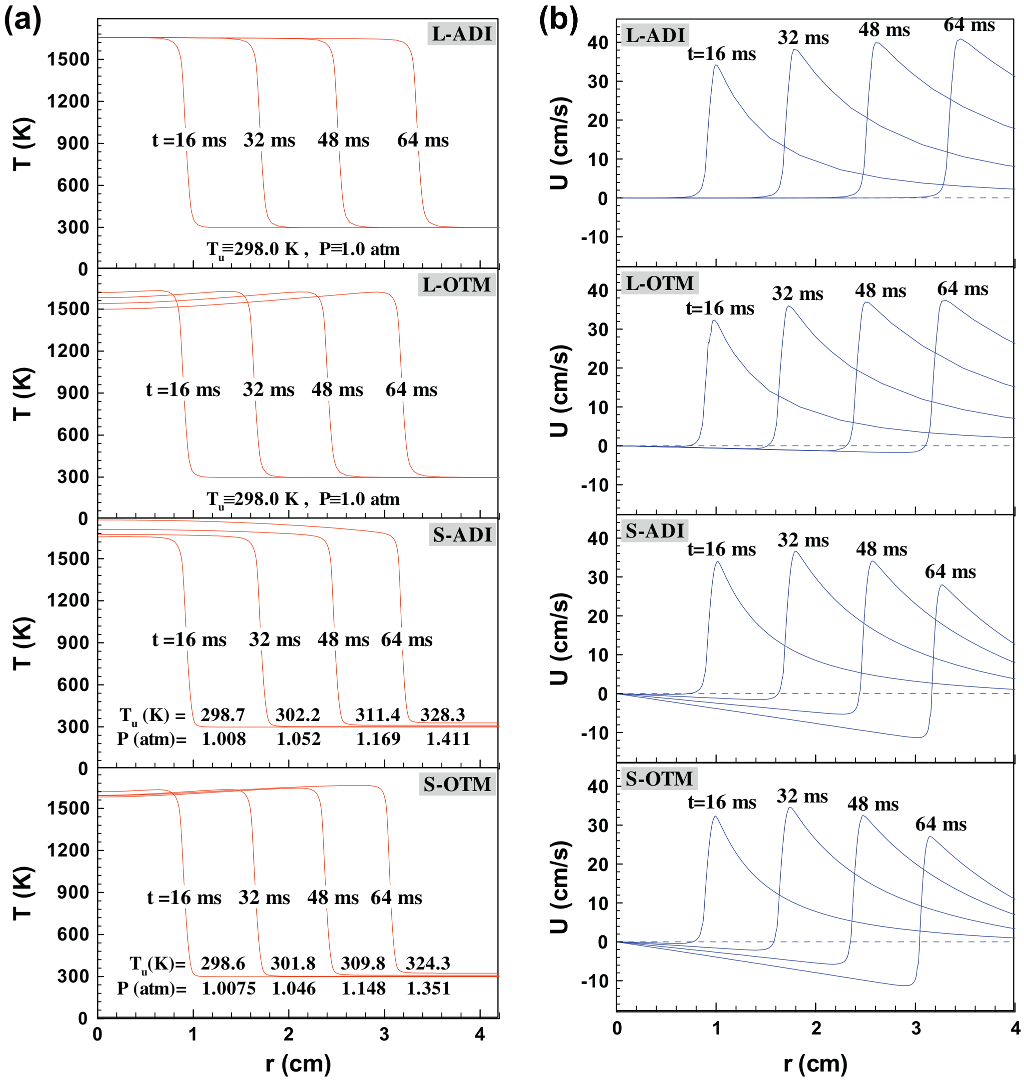

Fig. 4. Evolution of the distributions of: (a) temperature and (b) flow velocity for spherical methane/air ($\varphi = 0.585$) flames.

velocity of the experimentally visualized flame front was considered to be the burned flame speed, i.e. $S_b \approx S = dR_f/dt$. However, as shown in Figs. 4b and 5, the burned gas velocity is not zero when radiation or compression is considered. As a result, inaccurate S_u^0 and L_b will be obtained by assuming $S_b \approx S$ when radiation and/or compression effects are not negligible (for example, for lean CH_4/air flames propagating in a small chamber of $R_w = 4.86$ cm [26]). This will be demonstrated in the following.

3.2.1. Radiation effects

Figure 6 shows the effects of radiation on the linear extrapolation of S_b^0 and L_b for a lean methane/air mixture ($\varphi = 0.536$). Linear extrapolation is conducted based on simulation results with flame radius in the range of $1.5 \leqslant R_f \leqslant 2.5$ cm. Flames with larger flame radius ($R_f \geqslant 1.5$ cm) are used so that the effects of ignition and finite flame thickness [12,23] can be minimized. Without radiative loss (L-ADI), S_b is shown to change linearly with K and the extracted results are $S_b^0 = 35.1$ cm/s and $L_b = 0.88$ mm. When radiative loss is included (L-OTM), different values of S_b^0 and L_b can be extracted, depending on whether the radiation induced velocity is considered. Without considering U_b ($S_b \approx S$ for L-OTM), Fig. 6 shows that the extracted S_b^0 and L_b are 14% and 50% lower, respectively. This is caused by the coupling between the thermal and flow effects induced by radiation. When U_b is considered ($S_b = S - U_b$ for L-OTM), the extracted S_b^0 and L_b are shown to be 8% and 6% lower, respectively. This is caused by the thermal effect only. Therefore, the laminar flame speed and Markstein length extracted from the linear extrapolation are both reduced by the thermal and flow effects induced by radiation.

The laminar flame speed and Markstein length of CH_4/air mixtures ($0.5 \leqslant \varphi \leqslant 0.6$) extracted from different linear extrapolations are shown in Fig. 7. The thermal and flow effects are indicated in Fig. 7. It is seen that the thermal effect on the extracted S_u^0 and L_b decreases with the equivalence ratio. This is because the relative reduction of the flame temperature by radiative loss decreases with φ. The flow effect on the extracted S_u^0 and L_b is also shown to decrease with φ. This is due to the fact that the stretch rate at the same flame radius increases with φ (thus the flow effect on linear extrapolation becomes weaker for larger φ). The results shown in Fig. 7 indicate that the radiation effects cause 7% (for $\varphi = 0.6$) to 25% (for $\varphi = 0.5$) under-prediction of S_u^0, and 38% (for $\varphi = 0.6$) to 62% (for $\varphi = 0.5$) under-prediction of L_b. The measured laminar flame speeds and Markstein lengths of CH_4/air mixtures near the lean flammability limit are strongly affected by radiation. Therefore, the laminar flame speed and Markstein length measured in the micro-gravity experiments [26,32] are shown to be much lower than those predicted by numerical simulation (see Figs. 1 and 7).

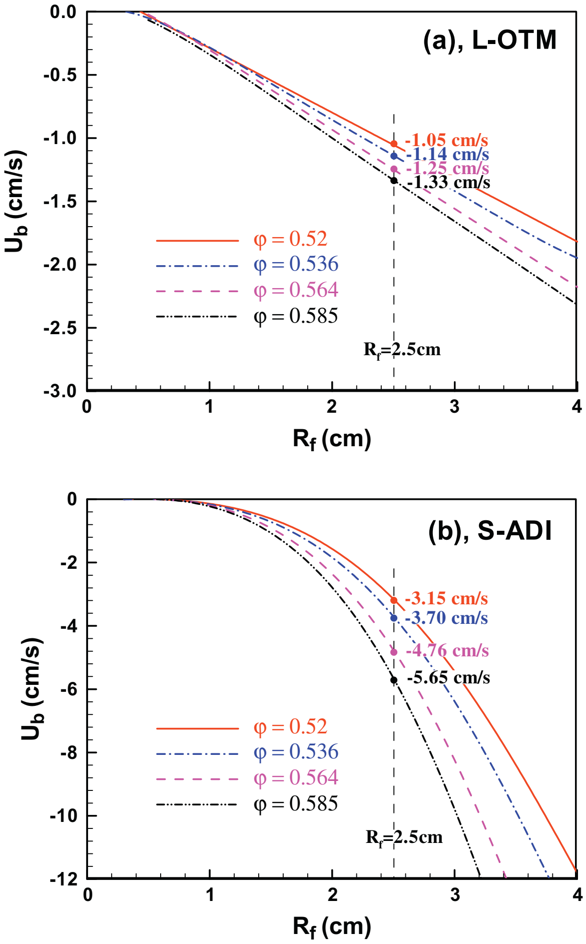

Fig. 5. Change of the burned gas flow velocity with the flame radius: (a) inward flow caused by radiation (L-OTM); and (b) inward flow caused by compression (S-ADI).

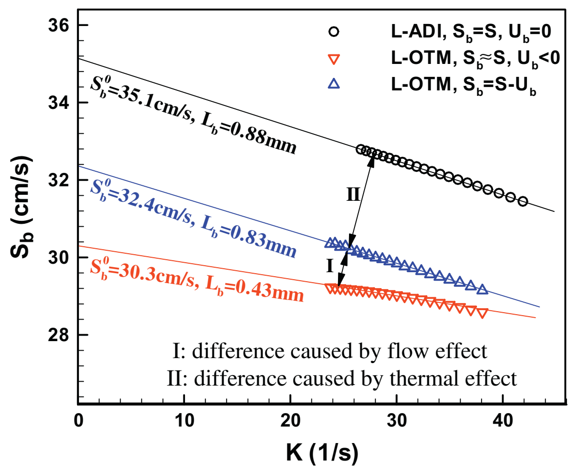

Fig. 6. Effects of radiation on the stretched flame speed of spherical methane/air (φ = 0.536) flames. Symbols: results from simulation with flame radius in the range of $1.5 \leqslant R_f \leqslant 2.5$ cm; lines: linear extrapolations.

The results shown in Figs. 6 and 7 are from linear extrapolations using flames with radius in the range of $1.5 \leqslant R_f \leqslant 2.5$ cm. However, as shown in Fig. 5a, the absolute value of U_b changes with R_f. Therefore, the extracted results, S_u^0 and L_b, will be affected by the flame radius range employed in the linear extrapolation. This is demonstrated by Fig. 8, which presents S_u^0 and L_b from linear

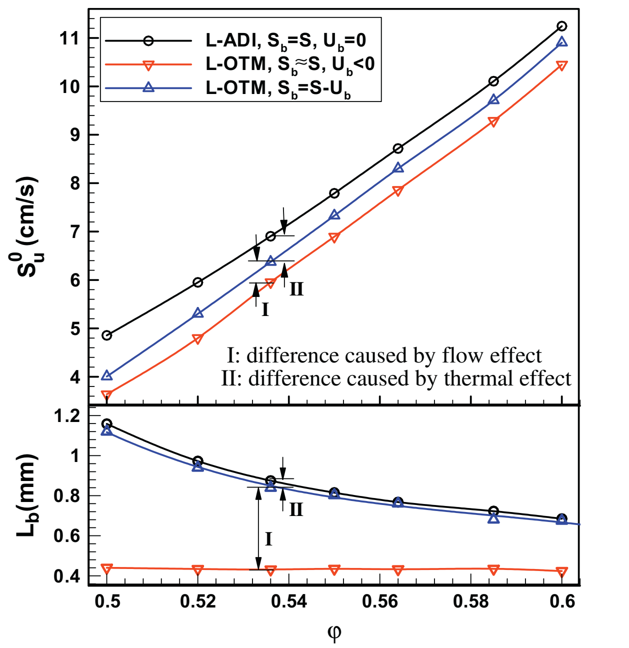

Fig. 7. Effects of radiation on the laminar flame speed and Marksein length of methane/air mixtures near the lean flammability limit.

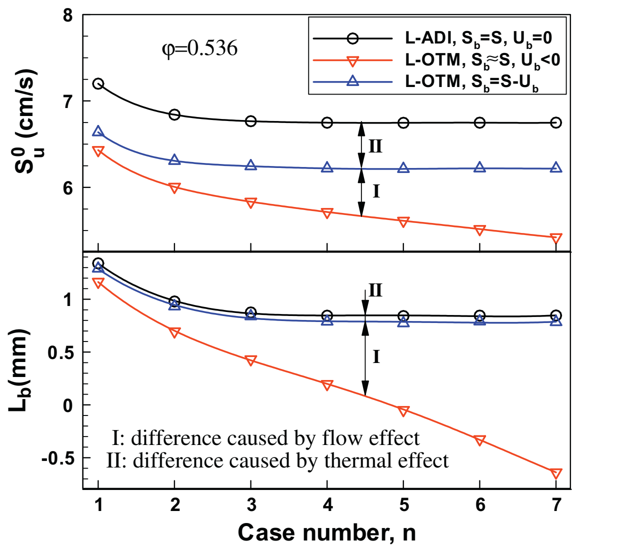

Fig. 8. Laminar flame speed and Markstein length from linear extrapolations using different flame radius ranges. The flame radius range for case number n is $0.5n \leqslant R_f \leqslant (0.5n + 1.0)$ cm.

extrapolations using different flame radius ranges. A case number, n, is introduced here to specify the flame radius range used in the linear extrapolation. For case number n, the corresponding flame radius range is $0.5n \leqslant R_f \leqslant (0.5n + 1.0)$ cm. Therefore, for a larger case number n, flames with larger flame radii are considered in the linear extrapolation. For the adiabatic case (L-ADI), there is obvious change in the extracted S_u^0 and L_b from case $n = 1$: $0.5 \leqslant R_f \leqslant 1.5$ cm to case $n = 2$: $1.0 \leqslant R_f \leqslant 2.0$ cm. This is because the flame propagation is affected by ignition and unsteadiness when the flame radius is small [23]. For $n > 2$, the extracted S_u^0 and L_b are shown to be independent of the flame radius range. However, when radiation is included (L-OTM), the extracted S_u^0 and L_b are shown to decrease with the flame radius range if U_b is not considered ($S_b \approx S$). This is because $|U_b|$ increases with R_f for L-OTM (Fig. 5a) and the linear extrapolation is more strongly

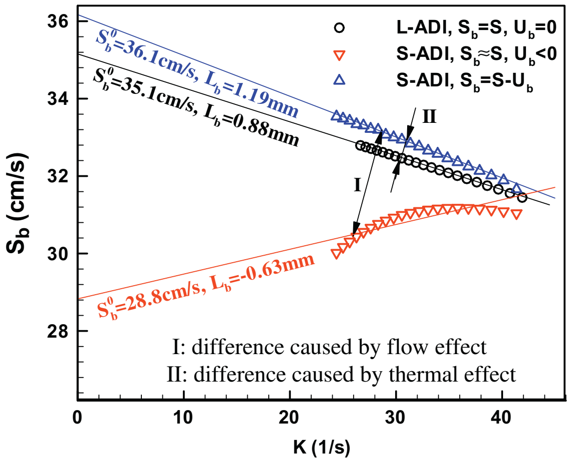

Fig. 9. Effects of compression on the stretched flame speed of spherical methane/air ($\varphi = 0.536$) flames. Symbols: results from simulation with flame radius in the range of $1.5 \leqslant R_f \leqslant 2.5$ cm; lines: linear extrapolations.

affected by the flow effect induced by radiation for flames with larger flame radii. When U_b is considered ($S_b = S - U_b$ for L-OTM), Fig. 8 shows that the extracted S_u^0 and L_b are also independent of the flame radius range for $n > 2$. Therefore, if the flow effect induced by radiation is not considered (L-OTM, $S_b \approx S$, $U_b < 0$), the measured laminar flame speeds and Markstein lengths will strongly depend on the flame radius range used in the linear extrapolation.

3.2.2. Compression effects

Similar to Fig. 6, Fig. 9 shows the compression effects on the linear extrapolation. When the compression is included and U_b is not considered ($S_b \approx S$ for S-ADI), the extracted S_b^0 and L_b are shown to be, respectively, 18% and 172% lower than those without compression ($S_b^0 = 35.1$ cm/s and $L_b = 0.88$ mm). This is caused by the coupling between the thermal and flow effects induced by compression. When U_b is considered ($S_b = S - U_b$ for S-ADI), the extracted S_b^0 and L_b are shown to be 3% and 35% higher, respectively. This is caused by the thermal effect by which the unburned gas temperature increases due to compression. Therefore, the laminar flame speed and Markstein length from linear extrapolation are both increased/decreased by the thermal/flow effect. Since the flow effect dominates over the thermal effect, both S_b^0 and L_b are reduced due to compression.

The laminar flame speed and Markstein length from different linear extrapolations are shown in Fig. 10. It is seen that the thermal effect on the extracted S_u^0 and L_b decreases with the equivalence ratio. This is because the relative change of the laminar flame speed due to unburned gas temperature rise decreases with φ. Unlike the thermal effect, the flow effect on the extracted S_u^0 and L_b is shown to increase with φ. This is because, at the same flame radius, the pressure changing rate, dP/dt, and thus the compression induced velocity, $|U_b|$, increase with φ for lean CH_4/air mixtures (see Fig. 5b). The results shown in Fig. 10 indicate that the compression effects cause 15% (for $\varphi = 0.5$) to 20% (for $\varphi = 0.6$) under-prediction of S_u^0, and 117% (for $\varphi = 0.5$) to 241% (for $\varphi = 0.6$) under-prediction of L_b. Therefore, the measured laminar flame speed and Markstein length of CH_4/air mixtures near the lean flammability limit are also greatly affected by compression.

Our previous study [35] showed that the pressure rise and thus the compression effects are proportional to the cube of the normalized flame radius, $(R_f/R_w)^3$. Therefore, for a given flame radius range (for example $1.5 \leqslant R_f \leqslant 2.5$ cm), the compression effects strongly depend on the chamber size, R_w. Figure 11 shows the effects of chamber

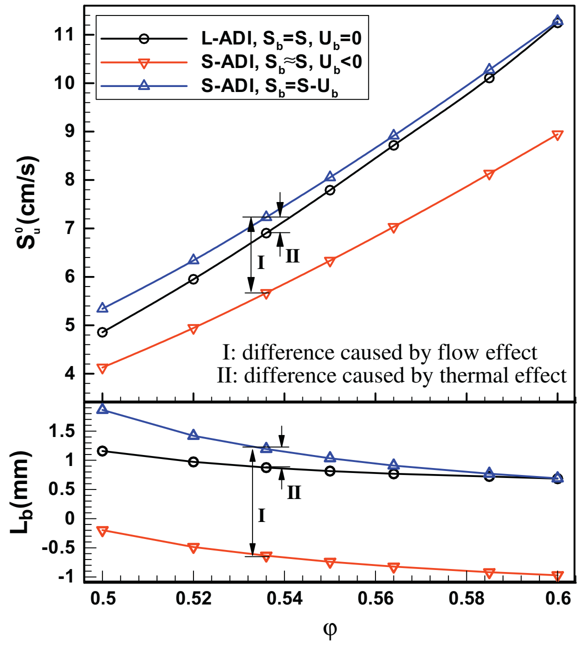

Fig. 10. Effects of compression on the laminar flame speed and Marksein length of methane/air mixtures near the lean flammability limit.

size on the extracted S_u^0 and L_b. It is seen that the thermal and flow effects induced by compression both decrease with the chamber size. When $R_w \geqslant 20$ cm, S_u^0 and L_b extracted from the linear extrapolation almost do not change with R_w. Therefore, the compression effects can be neglected for $R_w \geqslant 20$ cm. For $R_w = 10$ cm, Fig. 11 shows that S_u^0 is $1–6.75/6.90 = 2\%$ under-predicted while L_b is $1–0.69/0.87 = 20\%$ under-predicted due to compression effects. The much larger difference for L_b than that for S_u^0 is because the former is much more sensitive to the linear extrapolation and more difficult to be accurately extracted than the latter [30]. Therefore, in order to exclude the compression effects and thus to obtain accurate laminar flame speed and Markstein length, a chamber with radius not less than 10 cm should be employed in experiments. For the micro-gravity experiments conducted by Wang et al. [26], the

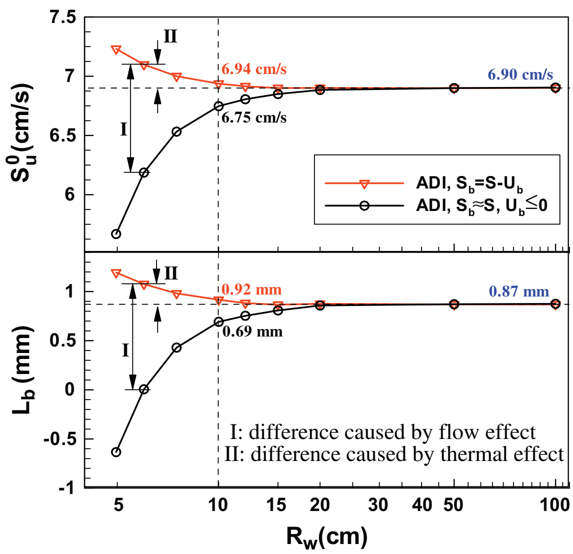

Fig. 11. Effects of chamber size (R_w) on the extracted laminar flame speed and Markstein length of methane/air mixture with $\varphi = 0.536$. The flame radius range used for linear extrapolation is $1.5 \leqslant R_f \leqslant 2.5$ cm.

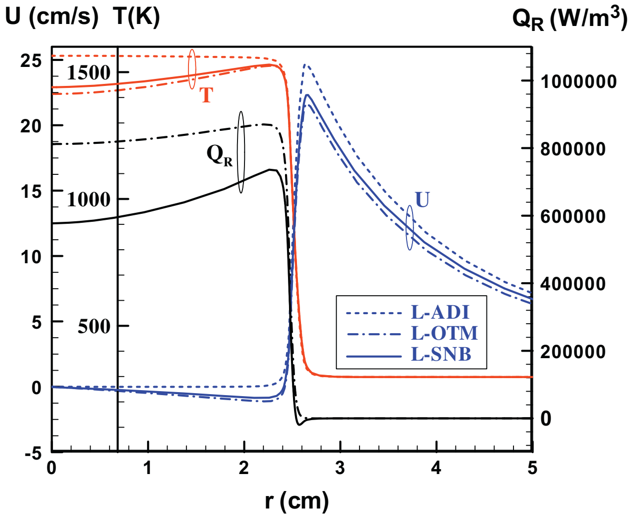

Fig. 12. Distributions of temperature, flow velocity, and volumetric radiative loss rate of a propagating spherical methane/air (φ = 0.536) flame with R_f = 2.5 cm.

equivalent chamber radius is 4.96 cm. Therefore, the laminar flame speed and Markstein length measured in Ref. [26] are much lower than those predicted by numerical simulation (see Figs. 1 and 10).

3.3. Effects of radiation re-absorption

In the Section 3.1, the optically thin model (OTM) is used and only radiative emission is considered. However, for mixtures near the flammability limit, the radiation re-absorption is important [42,44]. In the following, the effects of radiation re-absorption on lean CH_4/air flames are investigated via comparison among results from L-ADI, L-OTM, and L-SNB.

Figure 12 shows the distributions of temperature, flow velocity, and volumetric radiative loss rate of a propagating spherical methane/air (φ = 0.536) flame at R_f = 2.5 cm. It is seen that when radiation re-absorption is considered (L-SNB), the volumetric radiative loss rate is reduced by around 20%. Consequently, the flame temperature predicted by L-SNB is shown to be slightly higher than that by S-OTM, and the burned gas velocity ($|U_b|$) predicted by L-SNB is slighter lower than that by S-OTM. Therefore, the thermal and flow effects induced by radiation are both reduced when radiation re-absorption is considered. This is further demonstrated by Fig. 13 which shows S_b as a function of R_f or K for the same methane/air mixture (φ = 0.536). Figure 13a shows that at the same flame radius R_f, the flame speed (S or $S_b = S\text{-}U_b$) from L-SNB is larger than that from L-OTM due to radiation re-absorption. Therefore, the radiation effects on flame propagation speed are reduced when radiation re-absorption is considered. Moreover, the linear extrapolation results in Fig. 13b show that S_b^0 and L_b from L-SNB are closer to those from L-ADI than L-OTM. Therefore, the radiation effects on the linear extrapolation are also reduced when radiation re-absorption is considered.

The effects of different radiation models, OTM and SNB, on the unstretched laminar flame speed of lean methane/air mixtures are shown in Fig. 14. The thermal and flow effects for OTM and SNB are indicated in the figure. For φ = 0.65 (mixture far from the flammability limit), the relative reduction of the laminar flame speed, S_u^0, is 5.1% (1.9% due to thermal effect and 3.2% due to flow effect) when only radiative emission is considered (OTM), and 4.2% (1.6% due to thermal effect and 2.6% due to flow effect) when radiation re-absorption is considered (SNB). However, for φ = 0.5 (mixture close to the flammability limit—φ_{limit} = 0.468 predicted by simulation

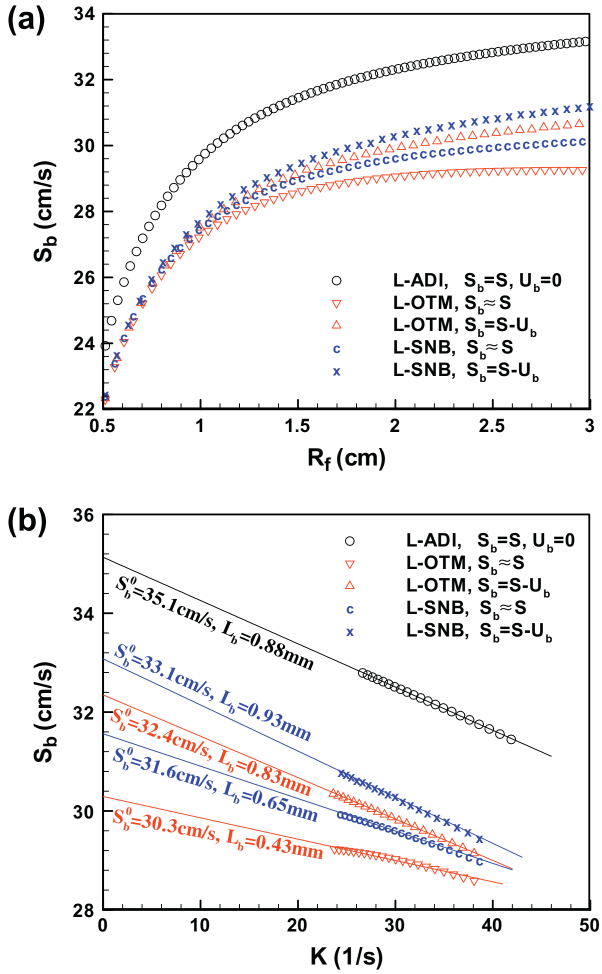

Fig. 13. Change of stretched flame speed relative to the burned gas with: (a) flame radius and (b) stretch rate of spherical methane/air (φ = 0.536) flames. The lines stand for linear extrapolations for which the flame radius range is 1.5 ⩽ R_f ⩽ 2.5 cm.

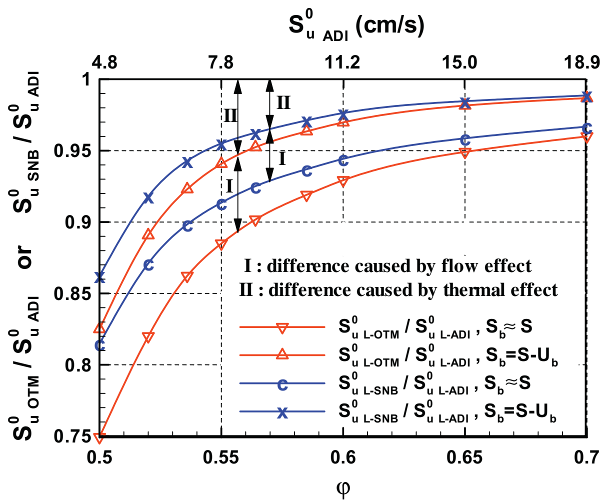

Fig. 14. Effects of different radiation models, OTM and SNB, on the unstretched laminar flame speed of methane/air mixtures near the lean flammability limit. The flame radius range used for linear extrapolation is 1.5 ⩽ R_f ⩽ 2.5 cm.

[45]), the relative reduction of S_u^0, is 24.9% (17.3% due to thermal effect and 7.6% due to flow effect) for OTM and 18.4% (13.6% due to thermal effect and 4.8% due to flow effect) for SNB. Therefore, as expected, the effects of radiation re-absorption become more

important for CH_4/air mixture closer to the lean flammability limit. Moreover, Fig. 14 shows that, for mixtures with $\varphi \geqslant 0.65$, the relative difference in S_u^0 caused by radiation re-absorption is within 1%. Therefore, the effects of radiation re-absorption can be neglected for lean CH_4/air mixtures with $\varphi \geqslant 0.65$.

As shown in this section, the burned gas velocity, U_b, is very important for the proper interpretation of results. However, it is practically impossible to measure U_b. Moreover, given the sensitivity of the results to the radiation model used (Fig. 14) and that potentially important radiation effects (absorption at the wall) are not taken into account in this study, it is also difficult to accurately predict U_b via numerical simulation. Therefore, in spherical flame experiments measuring the laminar flame speed and Markstein length, measures should be taken to minimize the radiation and/or compression induced flow.

4. Conclusions

Numerical simulations of propagating spherical flames of methane/air mixtures near the lean flammability limit are conducted. The effects of radiation and compression are assessed by changing the radiation model and the spherical chamber size. The main conclusions are:

1. Both radiation and compression strongly affect the flame propagation speed (S) and the extracted laminar flame speed (S_u^0) and Markstein length (L_b) from linear extrapolation. It is found that the reduction of the flame propagation speed is caused by the coupling between the thermal effect (change of flame temperature or unburned gas temperature) and flow effect (inward flow of burned gas, $U_b < 0$) induced by radiation or compression. The thermal and flow effects induced by radiation both reduce the flame speed. However, the thermal/flow effect induced by compression increases/decreases the flame speed. Since the flow effect dominates over the thermal effect, the flame speed is also reduced due to compression.
2. For methane/air mixtures with equivalence ratio between 0.5 and 0.6, it is shown that the radiation effects cause 7–25% under-prediction of S_u^0, and 38–62% under-prediction of L_b, while the compression effects cause 15–20% under-prediction of S_u^0, and 117–241% under-prediction of L_b. In the micro-gravity experiments for ultra-lean CH_4/air mixtures [26,32], the radiation and compression effects both exist but were not accounted for in the interpretation of the experimental measurements. Therefore, the extracted laminar flame speed and Markstein length reported in Refs. [26,32] are much lower than results from simulation and/or other measurements (see Fig. 1). As a result, the micro-gravity experiment results in Refs. [26,32] cannot not be used for kinetic mechanism validation.
3. In order to obtain accurate laminar flame speed and Markstein length from spherical flame experiments, the effects of radiation and compression should be minimized. The radiation effects on the extracted laminar flame speed and Markstein length are found to depend on the flame radius range used for linear extrapolation. In order to minimize the radiation effects, propagation speed at small flame radius should be used in data processing. The compression effects are shown to strongly depend on the chamber size. In order to exclude the compression effects, a chamber with radius not less than 10 cm should be employed for methane/air mixtures at normal temperature and pressure.
4. The thermal and flow effects induced by radiation are both reduced when radiation re-absorption is considered. Consequently, the radiation effects on the flame propagation speed (S) and the extracted laminar flame speed (S_u^0) and Markstein length (L_b) are reduced by radiation re-absorption. The effects of radiation re-absorption are found to become more important for CH_4/air mixture closer to the lean flammability limit. For lean CH_4/air mixtures with $\varphi \geqslant 0.65$, the relative difference in S_u^0 caused by radiation re-absorption is within 1% and thus the effects of radiation re-absorption can be neglected.

Acknowledgments

This work was supported by National Natural Science Foundation of China (Grant No. 50976003) and State Key Laboratory of Engines at Tianjin University (Grant No. K2010-02). We thank the referees for providing constructive comments and help in improving the paper.

References

[1] P. Clavin, Prog. Energy Combust. Sci. 11 (1985) 1–59.
[2] F.A. Williams, Combustion Theory, Benjamin-Cummins, Menlo Park, CA, 1985.
[3] C.K. Law, C.J. Sung, H. Wang, T.F. Lu, AIAA J. 41 (2003) 1629–1646.
[4] N. Peters, Turbulent Combustion, Cambridge University Press, New York, 2000.
[5] G.E. Andrews, D. Bradley, Combust. Flame 18 (1972) 133–153.
[6] C.J. Rallis, A.M. Garforth, Prog. Energy Combust. Sci. 6 (1980) 303–329.
[7] C.K. Wu, C.K. Law, Proc. Combust. Inst. 20 (1985) 1941–1949.
[8] Y. Huang, C.J. Sung, J.A. Eng, Combust. Flame 139 (2004) 239–251.
[9] D.R. Dowdy, D.B. Smith, S.C. Taylor, A. Williams, Proc. Combust. Inst. 23 (1990) 325–332.
[10] S.C. Taylor. Burning Velocity and the Influence of Flame Stretch. Ph.D. Thesis, University of Leeds, 1991.
[11] L.K. Tseng, M.A. Ismail, G.M. Faeth, Combust. Flame 95 (1993) 410–426.
[12] D. Bradley, P.H. Gaskell, X.J. Gu, Combust. Flame 104 (1996) 176–198.
[13] D. Bradley, R.A. Hicks, M. Lawes, C.G.W. Sheppard, R. Woolley, Combust. Flame 115 (1998) 126–144.
[14] M.I. Hassan, K.T. Aung, G.M. Faeth, Combust. Flame 115 (1998) 539–550.
[15] S.D. Tse, D.L. Zhu, C.K. Law, Proc. Combust. Inst. 28 (2000) 1793–1800.
[16] X.J. Gu, M.Z. Haq, M. Lawes, R. Woolley, Combust. Flame 121 (2000) 41–58.
[17] G. Rozenchan, D.L. Zhu, C.K. Law, S.D. Tse, Proc. Combust. Inst. 29 (2003) 1461–1470.
[18] F. Halter, C. Chauveau, N. Djeballi-Chaumeix, I. Gokalp, Proc. Combust. Inst. 30 (2005) 201–208.
[19] Z. Huang, Y. Zhang, K. Zeng, B. Liu, Q. Wang, D.M. Jiang, Combust. Flame 146 (2006) 302–311.
[20] L. Qiao, Y. Gu, W.J.A. Dam, E.S. Oran, G.M. Faeth, Combust. Flame 151 (2007) 196–208.
[21] Z. Chen, X. Qin, Y.G. Ju, Z.W. Zhao, M. Chaos, F.L. Dryer, Proc. Combust. Inst. 31 (2007) 1215–1222.
[22] E. Hu, Z. Huang, J. He, C. Jin, J. Zheng, Int. J. Hydrogen Energy 34 (2009) 4876–4888.
[23] Z. Chen, M.P. Burke, Y. Ju, Proc. Combust. Inst. 32 (2009) 1253–1260.
[24] M.P. Burke, Z. Chen, Y. Ju, F.L. Dryer, Combust. Flame 156 (2009) 771–779.
[25] T. Tahtouh, F. Halter, C. Mounaïm-Rousselle, Combust. Flame 156 (2009) 1735–1743.
[26] S. Wang, H. Zhang, J. Jarosinski, A. Gorczakowski, J. Podfilipski, Combust. Flame 157 (2010) 667–675.
[27] S.G. Davis, J. Quinard, G. Searby, Combust. Flame 130 (2002) 112–122.
[28] S.G. Davis, J. Quinard, G. Searby, Combust. Flame 130 (2002) 123–136.
[29] J.T. Farrell, R.J. Johnston, I.P. Androulakis, SAE Paper, 2004-01-2936.
[30] Z. Chen, Int. J. Hydrogen Energy 34 (2009) 6558–6567.
[31] R.J. Kee, J.F. Grcar, M.D. Smooke, J.A. Miller, Sandia National Laboratory Report SAND85-8240, 1985.
[32] P.D. Ronney, H.Y. Wachman, Combust. Flame 62 (1985) 107–119.
[33] Z. Chen, Y. Ju, Combust. Theor. Model. 11 (2007) 427–453.
[34] Z. Chen, X. Gou, Y. Ju, Combust. Sci. Technol. 182 (2010) 124–142.
[35] Z. Chen, M.P. Burke, Y. Ju, Combust. Theor. Model. 13 (2009) 343–364.
[36] Z. Chen, M.P. Burke, Y. Ju, Proc. Combust. Inst. 33 (2010), doi:10.1016/j.proci.2010.05.005.
[37] R.J. Kee, F.M. Rupley, J.A. Miller, Sandia National Laboratory Report SAND89-8009B, 1989.
[38] G. Strang, SIAM J. Numeric. Anal. 5 (1968) 506–517.
[39] P.N. Brown, G.D. Byrne, A.C. Hindmarsh, SIAM J. Sci. Stat. Comput. 10 (1989) 1038–1051.
[40] G.P. Smith et al., <http://www.me.berkeley.edu/gri_mech/>.
[41] Y. Ju, H.S. Guo, F.S. Liu, K. Maruta, J. Fluid Mech. 379 (1999) 165–190.
[42] Z. Chen, X. Qin, B. Xu, Y.G. Ju, F.S. Liu, Proc. Combust. Inst. 31 (2007) 2693–2700.
[43] M. Sun, K. Takayama, J. Comput. Phys. 150 (1999) 143–180.
[44] K. Maruta, K. Abe, S. Hasegawa, S. Maruyama, J. Sato, Proc. Combust. Inst. 31 (2007) 1223–1230.
[45] Y. Ju, G. Masuya, P.D. Ronney, Proc. Combust. Inst. 27 (1998) 2619–2626.
[46] T. Poinsot, D. Veynante, Theoretical and Numerical Combustion, second ed., Edwards, 2005.